

Contents lists available at ScienceDirect

Carbon

journal homepage: www.elsevier.com/locate/carbon





Organic solvent transport through reduced graphene oxide membranes with controlled oxygen content

Hongzhe Chen ^a, Tongxi Lin ^{a,*}, Zeno Rizqi Ramadhan ^b, Aditya Rawal ^c, Yuta Nishina ^{d,e}, Amir Karton ^f, Xiaojun Ren ^{a,**}, Rakesh Joshi ^{a,***}

- ^a School of Materials Science and Engineering, University of New South Wales Sydney, NSW 2052, Australia
- ^b Electron Microscope Unit, University of New South Wales, Sydney, NSW 2052, Australia
- Mark Wainwright Analytical Centre, University of New South Wales, Kensington, NSW, 2052, Australia
- ^d Research Institute for Interdisciplinary Science, Okayama University, Kita-ku, Okayama 700-8530, Japan
- e Institute for Aqua Regeneration, Shinshu University, 4-17-1 Wakasato, Nagano 380-8553, Japan
- f School of Science and Technology, University of New England, Armidale, NSW 2351, Australia

ARTICLE INFO

Keywords: Graphene oxide Organic solvent nanofiltration

ABSTRACT

Recent advances in membranes based on 2-dimensional (2D) materials have enabled precise control over angstrom-scale pores, providing a unique platform for studying diverse mass transport mechanisms. In this work, we systematically investigate the transport of solvent vapors through 2D channels made of graphene oxide (GO) laminates with precisely controlled oxygen content. Using in-situ chemical reduction of GO with vitamin C, we fabricated reduced GO membranes (VRGMs) with oxygen content systematically decreased from 31.6 % (pristine GO) to 24.0 % (VRGM-maximum reduction). Vapor permeability measurements showed a distinct correlation between oxygen functional groups and solvent transport behaviour. Specifically, non-polar hexane exhibits 114 % of enhanced permeance through the reduced membranes with larger graphitic domains, while the permeance of water decreases by 55 %. With the support of density functional theory (DFT) simulations, we modelled the hydrogen-bond and dispersion complexes between the solvents and GO and calculated the complexation energies. The simulation results suggest that polar molecules interact with the oxygen functional groups of GO via a hydrogen-bond network, supporting in-plane transport. In contrast, van der Waals forces drive the transport of low-polarity solvents along the graphitic domains of the 2D channel in reduced GO membranes. Our findings provide potential strategies for future design of organic solvent nanofiltration membranes.

1. Introduction

Graphene oxide (GO)-based membranes have been intensively investigated as a selective barrier in various molecular sieving applications, including water purification [1–4], gas separation [5–9] and organic solvent nanofiltration (OSN) [10–13]. GO membranes (GOMs) are fabricated by layer-by-layer stacking of two-dimensional (2D) graphene oxide (GO) nanosheets, allowing mass transport through the 2D channels (interlayer spacing). It is well known that GO consists of pure graphitic and oxygen-functionalized graphitic regions[14–16], which contribute differently to the transport of molecules [17]. For example, the graphitic domains allow the frictionless movement of water

molecules [18–20], and the oxygenated functional groups (such as hydroxyl and epoxy) attract water molecules through hydrogen-bonding [21,22], leading to the expansion of GO interlayer spacing. In addition, understanding the transport of organic solvents via GOMs has also attracted broad interest[23–25]. Several strategies, including reduction [26], crosslinking [27], intercalation [13] and functionalization [28], have been applied to modify the GO nanochannels. Intrinsically, the permeance of organic solvents depends on the solvent molecule's properties and their interactions with the oxygen functional groups or graphitic domains on GOMs[29–32]. The oxygen content of GO may result in a variation of solvent-GO interactions, thus leading to a change in the molecular permeation rate[33–35]. Generally, polar solvents such

E-mail addresses: tongxi.lin@student.unsw.edu.au (T. Lin), xiaojun.ren@unsw.edu.au (X. Ren), r.joshi@unsw.edu.au (R. Joshi).

^{*} Corresponding author.

^{**} Corresponding author.

^{***} Corresponding author.

as water and ethanol can cause the expansion of GO nanochannels and the swelling of GOMs, leading to a high solvent permeation, and however, compromising the molecular sieving capabilities. For non-polar solvents, the weak interactions between solvent molecules and nanochannels result in a lower permeation. In order to better investigate solvent transport behaviors, it is crucial to gain a deeper understanding of the correlations between the features of GO nanochannels and solvent-GO interactions. A systematic investigation that combines experimental observations and theoretical simulations to quantify this dependence and understand the underlying mechanism remains a significant knowledge gap.

In this study, we present the influence of oxygen content in GO on the solvent transport through GOMs. We have used an in-situ membranebased chemical reduction using vitamin C (VC) to obtain precise control of oxygen content in GO while preserving the laminated structure during reduction processes. Based on our previous study, controlling the VC concentration in the feed solution enables precise control of the oxygen content (reduction degree) of GOMs and thus varies the interlayer spacing. As discussed in previous studies, the transport of solvent molecules in GO membranes involves both in-plane (2D nanochannel) and out-of-plane (pinhole) pathways due to the laminated structure [16,36]. To specifically investigate in-plane solvent molecule diffusion through the 2D nanochannels, we fabricated the laminated membranes with a relatively high thickness by using high GO and rGO mass loadings to minimize diffusion through pinholes and ensure a more controlled study of mass transport [16]. We have used multiple sensitive characterization techniques to measure the oxygen contents of GOMs and VC-reduced GO membranes (VRGM) and conducted vapor transmembrane permeation experiments by using a setup with higher experimental sensitivity and precision to observe the effect of oxygen content variation on the solvent permeating through in GOMs and VRGMs. We performed density functional theory (DFT) simulations to further study our experimental observations. The computational results provide significant insights into experimentally observed solvent transport phenomena, particularly by elucidating the molecular-level interplay between hydrogen-bonding and dispersion interactions, and how these affect permeance through pristine and reduced graphene oxide membranes (GOMs). This study enhances our understanding of solvent transport mechanisms in 2D capillaries and paves the way for advancements in organic solvent filtration-based applications using graphene oxide (GO)- based membranes.

2. Experimental

2.1. Membrane fabrication

Polyvinylidene fluoride (PVDF) substrates (0.2 µm pore size, 47 mm diameter) were purchased from the Sterlitech Co. Vitamin C (VC, Lascorbic acid), chlorobenzene (CB), ethanol, acetone, dimethyl sulfoxide (DMSO) and n-hexane were purchased from Sigma-Aldrich Co. Graphene oxide (GO) was purchased from NiSiNa Materials Co. The complete procedure for the preparation of GOMs and VC-reduced GOMs (VRGM) is described in our earlier work [37]. For this study, GOMs were prepared with a GO mass loading of 0.16 mg/cm² and VC concentrations of 0.005 mg/mL, 0.05 mg/mL, 0.5 mg/mL and 1 mg/mL, respectively, to make different sets of samples. VC solution was filtered through GOMs for 24 h, and the VRGMs that were obtained were dried in the air. Higher VC concentration in the feed solution can lead to a higher degree of reduction in the rGO membrane [37]. Accordingly, the samples in this work were named according to the membrane reduction degree based on the VC concentrations of the feed solutions. VRGM-Low, Medium, High and Max represent the VC-reduced GO membranes (VRGMs) prepared with 0.005 mg/mL, 0.05 mg/mL, 0.5 mg/mL and 1 mg/mL of VC used in the feed solutions. The schematic illustration of the chemical reduction of GOMs with VC is shown in Fig. S1.

2.2. Materials characterizations

Various analytical techniques were used to characterise the GOMs and VRGMs, including Fourier transform infrared spectroscopy (FT-IR), X-ray photoelectron spectroscopy (XPS), solid-state nuclear magnetic resonance (ss-NMR), scanning electron microscopy (SEM), transmission electron microscope (TEM), contact angle measurement, X-ray diffraction (XRD) and Raman spectroscopy. A detailed description of these methods is given in our previous work [37]. More importantly, the solid-state NMR was used in this study to investigate the chemical environment of carbon atoms via a Vega-400 MHz Bruker Neo NMR system.

2.3. Vapor permeation measurement

Vapor transmembrane permeation experiments were conducted using a customised setup consisting of a glass container with a 16 mm diameter aperture on a chemically resistant lid. In our typical procedure, the glass container is initially filled with 10 mL of deionized water or organic solvents. The GOM or VRGM is precisely cut to cover the aperture and sealed with epoxy glue. The container and lid are also sealed with epoxy glue to ensure a leakproof system. The effective membrane area that allows permeation is determined using ImageJ software. A schematic illustration is shown in Fig. S2. The container with solvent and membrane is placed on a highly sensitive computer-controlled weighing scale for precise weight loss measurements. The complete setup is placed in an airbag and continuously filled with nitrogen to maintain a stable, low-humidity environment.

3. Results and discussion

Before the solvent vapor permeation analysis, we study the oxygen content and structural properties of GO and rGO. GOMs were prepared with a GO mass loading of 0.16 mg/cm² and VC concentrations from 0.005 mg/mL to 1 mg/mL, leading to different reduction degrees [26, 37]. As detailed in the experimental section, samples were named VRGM-Low, Medium, High, and Max based on VC concentrations.

3.1. Chemical analysis

We systematically investigated the oxygen content in GO and the effect of reduction via vitamin C from a chemical analysis point of view. The FT-IR spectra of free-standing GO membranes (GOM) and vitamin Creduced GO membranes (VRGMs) are shown in Fig. 1a. The peaks at approximately 3200 cm⁻¹, 1725 cm⁻¹, 1620 cm⁻¹, 1410 cm⁻¹, 1320 cm⁻¹, 1220 cm⁻¹ and 1037 cm⁻¹ correspond to O-H stretching from water, C=O stretching from carboxyl groups, C=C stretching from sp²domains, O-H bending from carboxylic acids, C-H bending from alkanes, C-O-C stretching from epoxy groups, and C-O stretching from alcohols, respectively [38]. We observed that as the concentration of vitamin C increases, the intensities of O-H, C=O, and C-O-C bonds decrease significantly while the intensities of C=C and C-H bonds increase. Notably, compared to GOM, the O-H peak intensity of VRGM-Low decreased slightly, whereas the intensities of VRGM-Med, VRGM-High and VRGM-Max are reduced to a significantly low level, indicating that higher VC concentration in feed solutions can lead to a more significant removal of hydroxyl groups. In addition, similar trends in C=O and C-O-C removal can also be observed in the spectra. Here, intensities of C=C peaks increase with the addition of VC concentrations, indicating the restoration of sp² carbon in VRGMs.

We analysed the changes in oxygen content and chemical bonding on GOM and VRGMs using high-resolution XPS and survey scans. Our results show that with the addition of VC, the oxygen content decreases from 31.6 % for pure GOM (C/O ratio of 2.16) to 24.0 % for VRGM-Max (C/O ratio of 3.16). Here, VRGM-Max represents the highest reduction degree with the lowest oxygen content that can be obtained under this

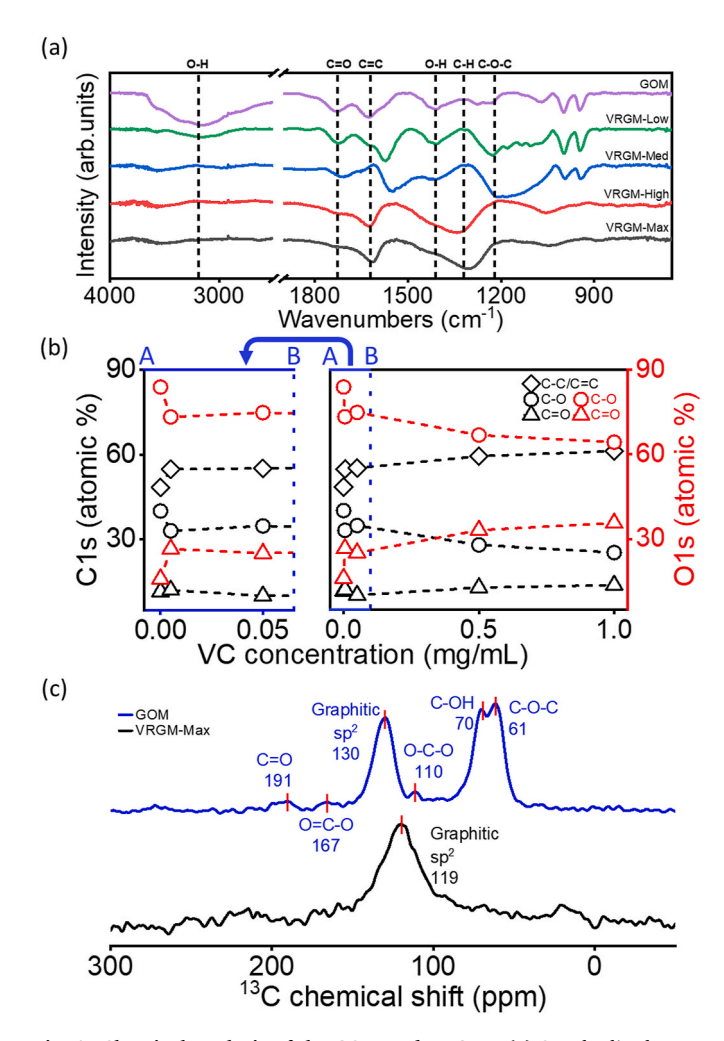


Fig. 1. Chemical analysis of the GOM and VRGMs. (a) Standardized FT-IR spectra of free-standing GOM and VRGMs. The vertical black dash lines indicate the peak position of O–H ($\sim\!3200~{\rm cm^{-1}}$ and $\sim\!1410~{\rm cm^{-1}}$), C=O ($\sim\!1725~{\rm cm^{-1}}$), C=C (1620 ${\rm cm^{-1}}$), C-H ($\sim\!1320~{\rm cm^{-1}}$) and C-O–C ($\sim\!1220~{\rm cm^{-1}}$) groups. (b) The variation of carbon (C1s) and oxygen (O1s) contents in atomic percentage with VC concentration of GOM and VRGMs.The blue arrow indicates the magnified image within the range of VC concentration from 0 to 0.1 mg/mL (c) $^{13}{\rm C}$ ss-NMR spectrum of GOM and VRGM-Max. The vertical red lines indicate the peak position of various carbon-carbon and carbon-oxygen bonds. (For interpretation of the references to color in this figure legend, the reader is referred to the Web version of this article.)

specific membrane-based chemical reduction method. Fig. 1b demonstrates the change in the atomic percentage of chemical bonds in GOM and VRGMs. Black and red legends represent the data extracted from C1s and O1s, respectively. Based on C1s spectra, with higher VC concentration, the C-C/C=C bonds show a general increase from 48.42 % of GOM to 61.20 % of VRGM-Max, while the C-O bonds show a decrease from 40.06 % to 25.16 %. According to O1s spectra, the C-O bond content for pure GOM is 83.94 %, however, with the increase of VC concentrations, it decreases from 73.36 % of VRGM-Low to 64.35 % of VRGM-Max. In contrast, the atomic percentage of the C=O bond shows a significant increase from 16.05 % for pure GOM to 35.64 % for VRGM-Max. The high-resolution XPS C1s and O1s spectra are shown in Fig. S3a and S3b, and the detailed data sheet is shown in Table S3. The binding energy shift in XPS spectra also provides important information. In C1s spectra, we observed that the C-O peak shifts slightly from 286.2 eV to 286.4 eV as the oxygen content decreases with increasing VC concentration, while the C-C/C=C and C=O peaks show no significant changes. In the O1s spectra, the C-O peak shifts from 532.3 eV to 532.9 eV, and

the C=O peak shifts from 531.0 eV to 531.8 eV with the same VC addition. The binding energy shift in C1s could be negligible. Meanwhile, in O1s spectra, the C-O peak and C=O peak shifts to a higher binding energy. This could result from changes in the surrounding chemical environment, especially the removal of nearby electron-donating oxygen functional groups during the reduction process. These observations support the view that the remaining oxygen atoms are in a more electron-deficient, and more graphitized environment.

We used the ss-NMR technique to confirm further the decrease in oxygen content and the transformation of the chemical environment during the reduction process. The ss-NMR spectra of GOM and VRGM-Max are shown in Fig. 1c. The peaks at 61 ppm, 70 ppm, 110 ppm, 130 ppm, 167 ppm and 191 ppm, represent the C-O-C from epoxy rings, C-OH from hydroxyl groups, O-C-O from lactols, graphitic sp²-hybridized carbons, O=C-O from acid/esters and C=O from ketones, respectively [39]. In the NMR spectrum for VRGM-Max, the distinct peak at 119 ppm represents the aromatic carbon. The significant reduction of oxygenated carbon peaks suggests the reduction of oxidized carbon functional groups. The signal of the aromatic carbons in GOM has the expected chemical shift of ~130 ppm, and for the VRGM-Max the aromatic peak position is shifted significantly to lower chemical shifts of \sim 119 ppm. The reduced chemical shift of the aromatic carbon peak is consistent with the formation of large-scale condensed aromatic ring structures and demonstrates the reduction of the GO into a graphene-like structure [40].

3.2. Surface and material structure

We have observed that the VRGMs maintain their laminated structure by using SEM. Fig. 2a and b and S4a-c demonstrate the surface morphology of GOM and VRGMs. It can be seen that GOM exhibits a typical smooth surface, while aggregated wrinkles are present on the surface of VRGMs. In VRGM-Low, the size of the wrinkles is relatively small, and it significantly increased in VRGM-Med and VRGM-High. Fig. 2c and d and Figure S4d-f show the cross-sectional morphology of GOM and VRGMs. All membranes exhibit a well-defined layered structure. Also, it's interesting to see that the thickness of membranes gradually decreases from 583 nm (as observed in SEM) for pure GOM to 234 nm of VRGM-Max after reduction with the same GO loading amount. This reduction in thickness is due to the removal of functional groups of GO, which decreases the interlayer spacing, resulting in thinner membranes. The HRTEM images (Fig. 2e and f for GO and VRGM-Max) exhibit a flat sheet morphology that remains unchanged after the membrane-based reduction processes. The hexagonal spots and rings observed in Fast Fourier Transform (FFT) patterns demonstrate the presence of layered GO, ordered graphitic domains (for VRGM-Max) and disordered oxygen functional group regions [41,42]. As seen in the magnified HRTEM images of GO and VRGM-Max (in Fig. 2g and h), the lower and higher contrast areas represent graphitic domains and oxygen functional group regions, respectively [15,43]. Comparing GO with VRGM-Max (10 nm \times 10 nm) reveals that VRGM-Max exhibits a larger and more ordered graphitic domain area. This enlargement can be the restoration of sp² carbon after chemical reduction.

Fig. 3a presents the XRD patterns of the GOM and VRGMs in a dry state. For GOM, a distinct diffraction peak appears at 9.9° (d = 8.9 Å), corresponding to the (001) reflection plane [44]. The sharp and strong (001) signal indicates a highly ordered laminated structure of GOM. With the addition of VC, the (001) peaks of VRGMs shift to higher 20 values, accompanied by a noticeable increase of full width at half maximum (FWHM). The (001) peaks of VRGM-Low, VRGM-Med and VRGM-High are located at 10.79° (d = 8.2 Å), 11.97° (d = 7.4 Å), and 12.07° (d = 7.3 Å), respectively. The higher FWHM of the (001) peak of VRGM-Max shifts to approximately 23° (d = 3.9 Å) with a significantly large FWHM, indicating substantial removal of oxygen functional groups [45,46]. VRGM-Max exhibits the smallest interlayer spacing and

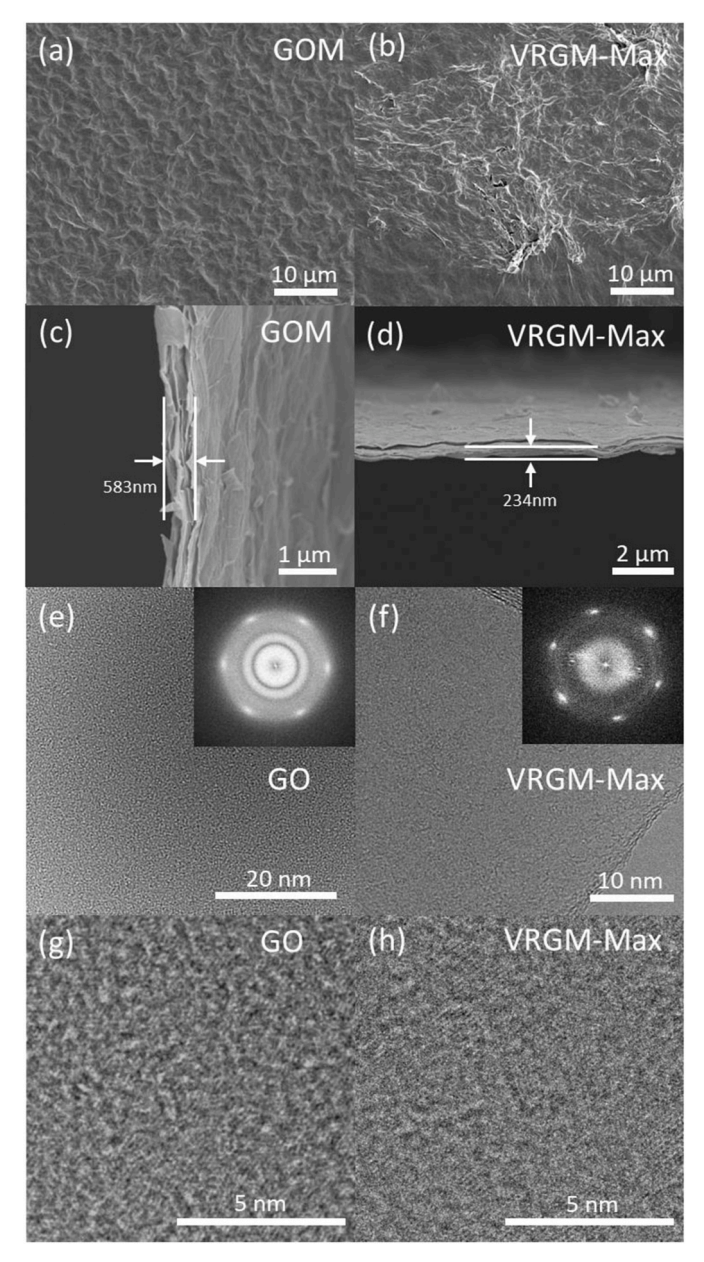


Fig. 2. Microscopy analysis of GOM and VRGMs. (a–b) SEM surface images of GOM (a) and VRGM-Max (b). (c-d) SEM cross-sectional images of GOM (c) and VRGM-Max (d). (e–h) HRTEM images of GO (e) and VRGM-Max (f) with insets of fast Fourier transform (FFT). Magnified HRTEM images of GO (g) and VRGM-Max (h).

the most disordered laminated structure among all membranes. It should be noted that during the VC reduction process, both types of disorder are present: chemical disorder resulting from the mild chemical reduction and the partial and random removal of oxygen-containing functional groups, and physical disorder due to changes in the membrane structure, such as wrinkling and collapse of the laminated structure. It is also worth noting that the value of interlayer spacing obtained from XRD patterns only represents the average and the most significant interlayer spacing of the membrane. These results reveal the removal of oxygen functional groups on GOMs after VC addition, which is further confirmed by the change of membrane hydrophilicity via contact angle measurements (Fig. S5). Fig. 3b shows the membrane's XRD d-spacing and water contact angle with VC concentrations, revealing that the variation of membrane hydrophilicity and interlayer spacing is closely correlated with the reduction degree. The higher reduction rate of GO

leads to lower membrane hydrophilicity, which is consistent with the study reported by Eda et al. [47]. The highest contact angle of VRGM-Max indicates its lowest hydrophilicity among all the membranes. The surface properties could also provide an insight into the chemical properties of the interlayer space and might offer information about how surface chemistry influences the behaviour of solvents within the nanochannels. To understand the swelling effect, we investigated the interaction of polar and non-polar solvents with the laminated structure of GOM and the highly reduced VRGM (VRGM-Max) using XRD analysis. Fig. S6a shows the (001) peak of GOM in different states: dry $(2\theta = 9.9^{\circ},$ d=8.9 Å), water-wetted ($2\theta=6.6^{\circ}$, d=13.4 Å) and hexane-wetted (2θ $= 9.7^{\circ}$, d = 8.3 Å). GOM exhibits significant swelling in water, increasing its d-spacing, while hexane causes negligible swelling with no significant change in d-spacing. Fig. S6b shows the XRD patterns of VRGM-Max in a dry, water-soaked and hexane-soaked state. The results indicate that XRD VRGM-Max membranes maintain their structure without detectable changes upon exposure to these solvents.

We used Raman spectroscopy to analyze the structure of GOM and VRGMs further and investigate the degree of disorder in prepared membranes. Fig. 3c-g and Fig. S7 show the Raman spectra of GOM and VRGMs. As illustrated in Fig. S7, the Raman spectra of all membranes exhibit characteristic D, G, 2D and D + G bands associated with GObased materials [26]. D-band is located at around 1344 cm⁻¹ and G-band at around 1604 cm⁻¹. The D-band corresponds to the sp³-hybridized carbon and disorder crystalline structure, while the G-band represents the sp²-hybridized carbon in graphene-based materials [48]. Additionally, the 2D-band and D + G band located at 2706 cm $^{-1}$ and 2919 cm⁻¹, respectively, correspond to layered stacking of GO based sheets [49]. We further analysed the Raman spectra to gain deeper insight into the molecular structure. The intensity ratio of the D-band to the G-band (I_D/I_G) is used to evaluate variations in boundaries, defects, and edges in GOM and VRGMs. The Raman spectrum of GOM and VRGMs in the first order was deconvoluted using four Lorentzian functions (D*, D, G, D') and one Gaussian function (D"). The detailed fitting parameters are shown in Table S4. Herein, we use AD", calculated using the integral area of peak D" divided by the total integral area of fitted spectra. Sadezky et al. have suggested that the value of AD" may indicate the degree of short-range order in carbon-based materials at a molecular level [50]. The variation in I_D/I_G ratio and the value of A_{D} , with VC concentrations is shown in Fig. 3h. We observed that the reduction of GOM to VRGM results in the increase of I_D/I_G ratios and, at the same time, a significant decrease in the value of AD". Cao et al. suggest that this occurs due to the enlarged graphitic domains on the rGO surface and the formation of smaller rGO sheets with boundaries and edges after reduction [51]. This observation is consistent with the XRD and contact angle analysis results, as discussed above.

Our overall analysis shows that our membranes have well-defined controlled graphitic domains and oxygen functional groups, making them suitable for studying solvent permeation.

3.3. Vapor permeation

We investigated the solvent transport properties of GO membranes (GOMs) and variably reduced graphene-based membranes (VGRMs). By precisely controlling the reduction process of VGRMs, we modulated the ratio of graphitic domains and oxygen-containing functional groups, enabling a systematic evaluation of their influence on solvent permeance. As described in the experimental section, we continuously monitored the weight loss of selected solvents in a sealed container as they permeated through GOMs and VGRMs in vapor form. In these experiments, we tested the permeation of six solvents with varying polarity indexes, including water, ethanol, DMSO, acetone, chlorobenzene, and hexane. The polarity index of the selected solvents is shown in Supplementary Note 1. The weight loss due to vapor permeating through the membrane was recorded regularly. Permeance (*P*), which is an intrinsic property of a specific membrane for a particular gas or vapor, is given by

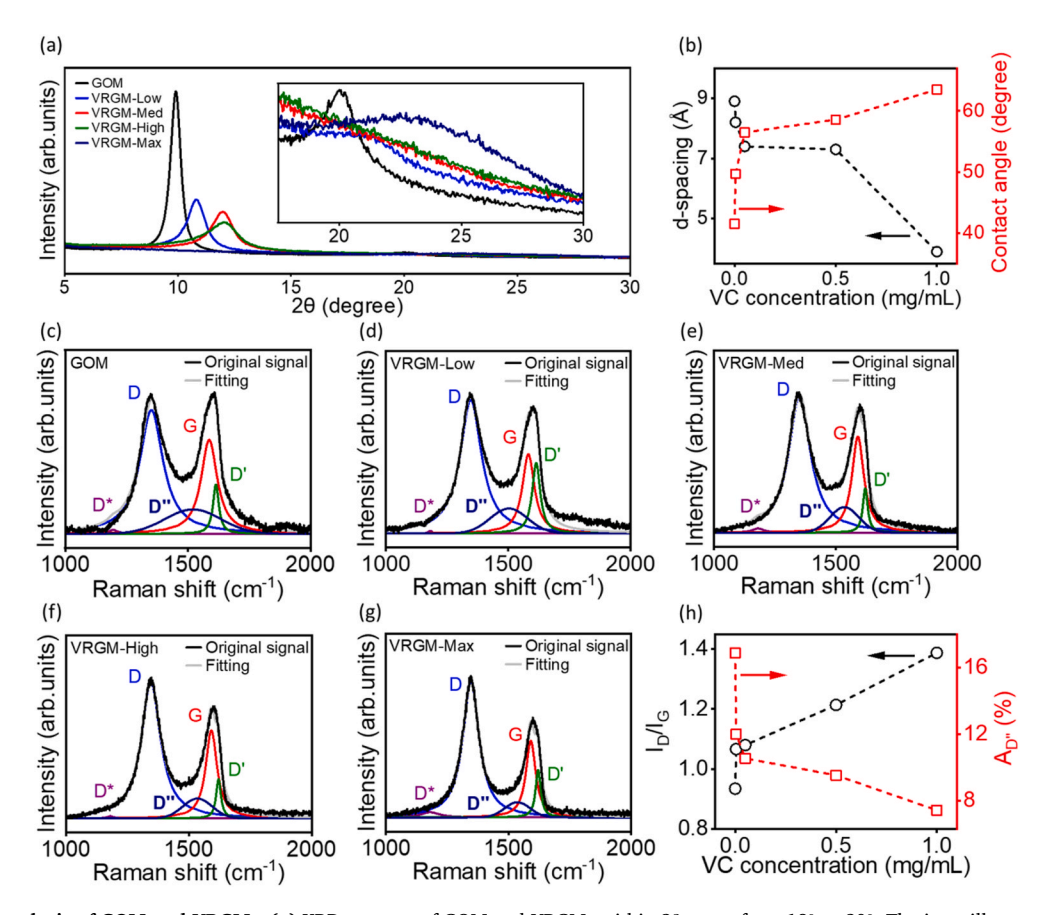


Fig. 3. Structural analysis of GOM and VRGMs. (a) XRD patterns of GOM and VRGMs within 2θ range from 18° to 30° . The inset illustrates the high-resolution patterns of (002) peaks. (b) Variation of d-spacing and water contact angle with VC concentration. (c–g) Raman spectra of GOM (c), VRGM-Low (d), VRGM-Med (e), VRGM-High (f) and VRGM-Max (g) and the fitting of the spectra. The fitted peaks are using four Lorentzian functions for D^* (\sim 1180 cm $^{-1}$), D (\sim 1590 cm $^{-1}$), D' (\sim 1620 cm $^{-1}$) and Gaussian function for D'' (\sim 1490 cm $^{-1}$) [52,53]. The detailed fitting parameters are shown in Table S4. (h) Variation of intensity ratio between peak D & D'' divided by the total integral area of fitted spectra.

Refs. [54,55]:

$$P = \frac{W}{tA_m(p_s - p_a)} \tag{1}$$

Where W is the weight loss of a specific solution (µmol), t is the duration of the experiment (h), A_m is the effective membrane area (mm²), measured by ImageJ (Supplementary Note 1). p_s is the solvent saturated vapor pressure (in bar). The saturated vapor pressures of different solvents are listed in Table S1; p_a is the atmospheric pressure of the airbag (bar) used during the weight loss measurement. Here, the solvent transport in GO-based laminated membranes follows Fick's law of diffusion via a tortuous layer-by-layer pathways [36]. Accordingly, the effect of membrane thickness on vapor permeance is primarily determined by the number of layers. Although the overall membrane thickness decreases from ~583 nm (GOM) to ~234 nm (VRGM-Max), the number of GO layers remains similar due to the corresponding reduction in interlayer spacing from 8.9 Å to 3.9 Å. This indicates that the vertical diffusion pathway, governed by the number of 2D nanochannels, remains largely intact. Additionally, since the laminated structure is maintained during the in-situ VC reduction process, the in-plane transport pathways also remain unchanged. Therefore, we do not attribute the changes in vapor permeance to the membrane thickness.

The selected solvents exhibit different permeation behaviours in GOMs and VGRMs. When GOMs were progressively reduced to VGRM-Med, and VGRM-Max, the membrane permeance of high polarity solvents (water, ethanol and DMSO) decreased significantly (Fig. 4a–c), consistent with previous studies [29,33]. In contrast, acetone,

chlorobenzene and hexane exhibit opposite trends when permeating through GOMs and VRGMs, as shown in Fig. 4d–f. Hexane has a much higher permeance in VGRM-Max compared with GOMs. The permeance of solvents via GOMs and VGRMs is summarised in Fig. 4g, showing an overall downward trend from the high to low polarity index. We further analysed the relationship between the oxygen content of the membranes and the permeance of various solvents (Fig. 4h). In particular, the permeance of water dramatically decreases as the oxygen functionalities are removed from GOMs, dropping from 1.19 μ mol/h/mm²/kPa of GOM to 0.65 μ mol/h/mm²/kPa of VRGM-Max, which is 55 %. This observation indicates that oxygen groups are crucial in facilitating the transport of high-polarity solvents through the membranes.

In the case of reduced graphene oxide, the possible interaction between high-polarity solvent molecules and the 2D channels will be less due to the missing functional groups. In this scenario, these solvent molecules are more likely to interact among themselves due to the nature of hydrogen-bond networks and dipole-dipole interactions. This interaction will result in the formation of solvent molecule clusters within the capillaries and hinder the mass transport thus resulting in the lower permeance of high polarity solvents [21,30,33]. The solvent molecules with low polarity (e.g., acetone, chlorobenzene and hexane) primarily interact with the graphitic regions on the GOMs via van der Waals forces. Removing functionalities increased the content of graphitic domains, further enhancing the frictionless movements of low-polarity solvent molecules and resulting in much higher permeance [36,56]. For example, the permeance of hexane increases from 0.0042 μ mol/h/mm²/kPa of GOM to 0.009 μ mol/h/mm²/kPa of VRGM-Max

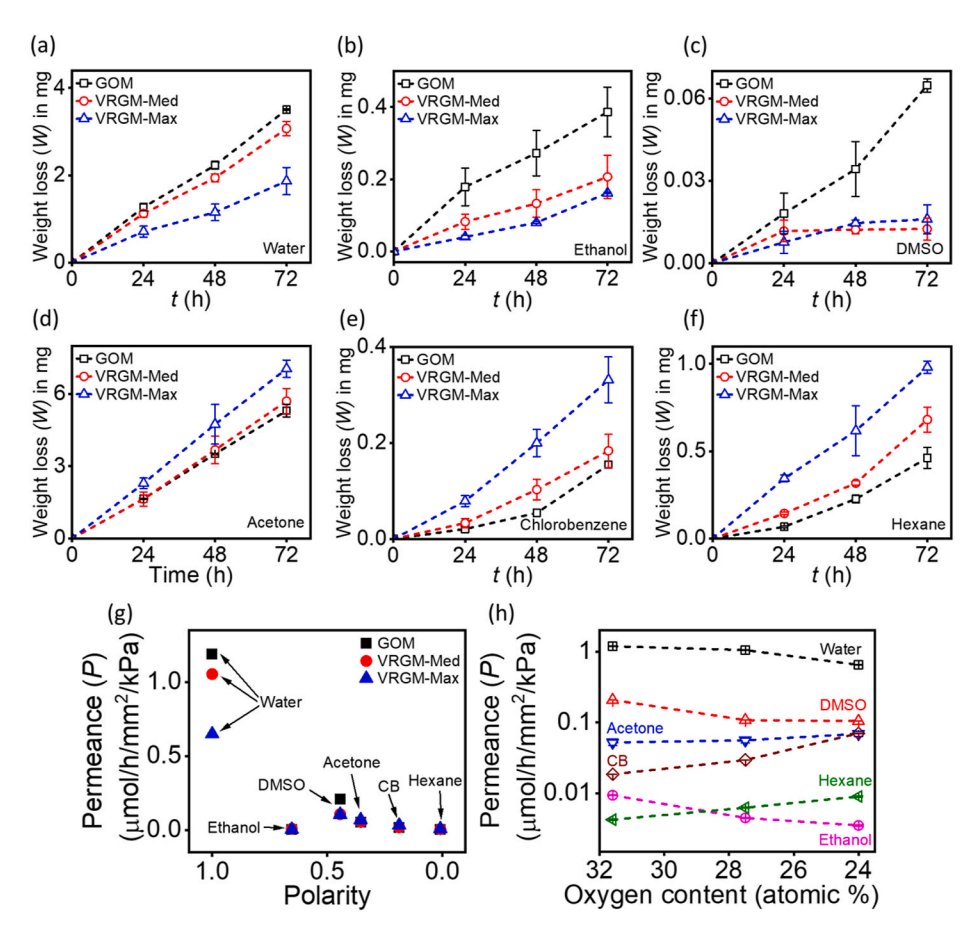


Fig. 4. Vapor permeation analysis. (a–f) Vapor permeation of water (a), ethanol (b), DMSO (c), acetone (d), CB (e), and hexane (f) through GOM, VRGM-Med and VRGM-Max. The short dash line is a guide to the eye. (g) The permeance of various organic solvents through GOM, VRGM-Med and VRGM-Max with solvent polarity Permeance (P) is calculated by equation (1); the polarity and saturated vapor pressure (P) of solvents are shown in Table S1, and P0 is measured pressure. (h) The permeance of different organic solvents through GOM, VRGM-Med and VRGM-Max as a function of oxygen content. The detailed data is shown in Table S2. The error bars are denoted by standard deviation.

(increase of 114 %).

3.4. DFT analysis of solvent-GO interactions

Density functional theory (DFT) calculations using the PW6B95-D3BJ/def2-QZVPP level of theory were performed to gain mechanistic insights into the experimental findings (see Computational Details Section in the Supplementary Note 8)[57-59]. The PW6B95 hybrid-meta generalized gradient approximation (GGA) exchange-correlation functional has been extensively benchmarked and found to provide excellent performance for thermochemistry, kinetics, and non-covalent interactions[60-68]. For full computational details, see the Supplementary Information. The experimental results indicate that as the GOM is reduced, i.e., there is a decrease in oxygen functional groups and an increase in the size of graphitic domains, the permeance of polar solvents that are able to act as a hydrogen-bond donor or acceptor (like water, ethanol, and DMSO) through the membrane decreases, while the permeance of non-polar solvents (like hexane and chlorobenzene) and acetone increases. These solvents can be divided into three classes. First, hydrocarbon-based solvents without OH and C=O functional groups that primarily interact with the graphitic domains via dispersion interactions, namely hexane and chlorobenzene. Second, organic solvents that can interact with both the graphitic domains via dispersion interactions and with the GO oxygen functional groups via H-bonding, namely ethanol, acetone, and DMSO. Third, one solvent that can primarily interact with the GO oxygen functional groups via H-bonding, namely water.

Fig. 5 displays the complexes between the solvents (water, ethanol, acetone, DMSO, chlorobenzene, and n-hexane) and the graphene-oxide models of epoxy and hydroxyl groups as well as the graphitic regions. Table 1 gives the PW6B95-D3BJ/def2-QZVPP interaction enthalpies $(\Delta H_{int,298})$ at 298 K for the complexes in Fig. 5. Let us begin with examining the dispersion interactions between the various solvents and the graphitic domains of GO (Fig. 5a and Table 1). The two solvents that exhibit significantly increased permeance with the increased availability of graphitic domains (hexane and chlorobenzene) exhibit significantly stronger dispersion interactions with the graphene flake (C54H18). In particular, we obtain $\Delta H_{\rm int,298} = -52.4$ (hexane) and -49.4 (chlorobenzene) kJ mol⁻¹, compared to interaction energies ranging between -18.3 and -35.5 kJ mol $^{-1}$ for the polar solvents. These results are in line with the experimental results, which demonstrate that hexane and chlorobenzene exhibit the most significant increase in permeance when moving from GOM to VRGM-Max (Fig. 4).

Let us move to considering water and ethanol that have hydrogenbond donating capabilities due to the presence of an OH group. These are the only solvents that can interact with both the GO-epoxy and GO-hydroxyl groups. The strength of the hydrogen-bond between water and GO is -13.8 (epoxy oxygen) and -19.8 (hydroxyl oxygen) kJ $\rm mol^{-1}$. These H-bond energies, despite being relatively small, are much larger than any possible London dispersion interactions with the graphitic regions of GO. Therefore, it is no surprise that the permeance of water decreases sharply when moving from GOM to VRGM-Max (Fig. 4). On the other hand, ethanol can interact with the epoxy oxygen, hydroxyl oxygen, and graphitic regions of GO. Table 1 reveals that the following

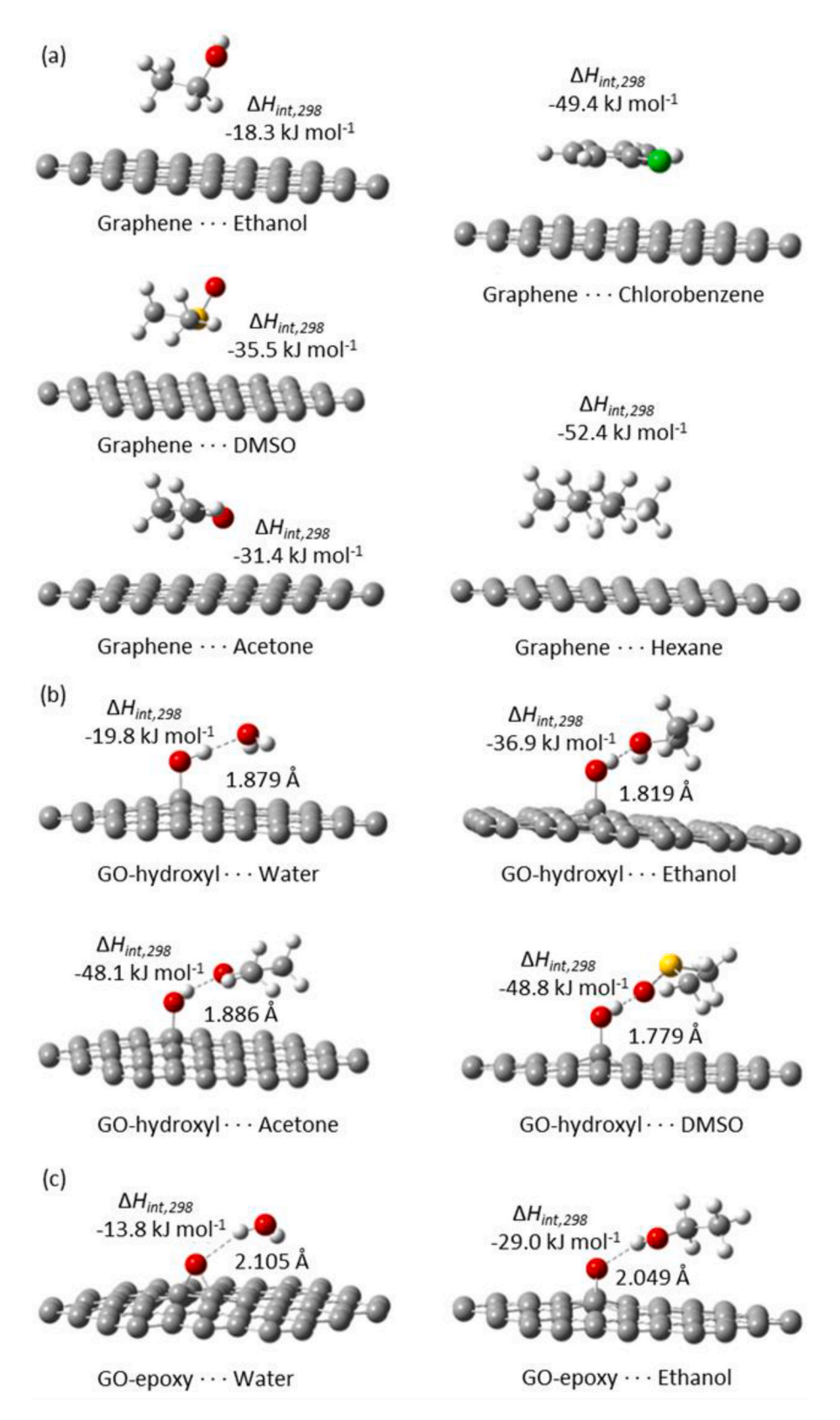


Fig. 5. Hydrogen-bond and dispersion complexes between the solvents considered in the present work and models of GO: (a) graphitic regions of GO, (b) GO-hydroxyl, and (c) GO-epoxy. Hydrogen-bonds are shown as dashed lines and hydrogen-bond distances are given in Å. Atomic color scheme: H, white; C, grey; O, red; S, yellow; for clarity the capping hydrogens of the GO model are removed. $\Delta H_{int,298}$ represents hydrogen-bond enthalpies. (For interpretation of the references to color in this figure legend, the reader is referred to the Web version of this article.)

Table 1 Calculated complexation energies on the enthalpic potential energy surface for the hydrogen-bond and dispersion complexes in Fig. 5. $\Delta H_{\rm int,298}$ values are calculated at the PW6B95-D3BJ/def2-QZVPP level of theory and given in kJ mol $^{-1}$.

Model		$\Delta H_{int,298}$ (kJ mol ⁻¹)
Graphene (5a)	Graphene Hexane	-52.4
	Graphene Chlorobenzene	-49.4
	Graphene DMSO	-35.5
	Graphene Acetone	-31.4
	Graphene Ethanol	-18.3
GO-hydroxyl (5b)	GO-hydroxyl DMSO	-48.8
	GO-hydroxyl Acetone	-48.1
	GO-hydroxyl Ethanol	-36.9
	GO-hydroxyl Water	-19.8
GO-epoxy (5c)	GO-epoxy Water	-13.8
	GO-epoxy Ethanol	-29.0

trend in terms of the magnitude of these interactions: GO-hydroxyl ($-36.9~\mathrm{kJ~mol}^{-1}$) > GO-epoxy oxygen ($-29.0~\mathrm{kJ~mol}^{-1}$) > GO-graphitic ($-18.3~\mathrm{kJ~mol}^{-1}$). Therefore, like water, ethanol exhibits the same trend in decreased permeance when moving from GOM to VRGM-max (Fig. 4).

Finally, let us consider the solvents (DMSO and acetone) that can interact with the GO-hydroxyl groups and graphitic domains, but not with the GO-epoxy groups (Fig. 5a-b). Both DMSO and acetone form very strong H-bonds with the GO-hydroxyl group, specifically, $\Delta H_{\rm int,298}$ = -48.8 and -48.1 kJ mol⁻¹, respectively (Table 1). It should be noted that these strong interactions reflect both H-bond and dispersion interactions with GO. These interaction enthalpies are considerably stronger than the dispersion interactions with the graphitic domains of GO, which amount to -35.5 and -31.4 kJ mol⁻¹ for DMSO and acetone, respectively. These computational results are consistent with the experimental results for DMSO where there is a sharp decrease in permeance when moving from GOM to either VRGM-med or VRGM-Max (Fig. 4). For acetone, however, the opposite experimental trend is observed (i.e., increased permeance upon reduction). This suggests that while the computational results confirm acetone's capability for strong hydrogen-bonding, its net transport behavior in the reduced membranes is ultimately more influenced by enhanced dispersion interactions. This highlights the complex interplay between dispersion and H-bonding interactions in determining overall solvent transport.

Overall, the DFT calculations provide strong mechanistic support at the molecular level for the experimental observations. Demonstrating the key roles and intricate interplay between dispersion and H-bonding interactions in determining overall solvent transport through pristine and reduced GO membranes.

4. Conclusions

We investigated the in-plane transport behaviors of polar and nonpolar solvents for GO membranes (GOMs) and vitamin C-reduced GO membranes (VRGMs). We observed that the hydrogen-bond network and van der Waals force interactions influence solvent vapor transport in GO-based 2D channels through the regions with oxygen functional groups and graphitic domains, respectively. The structural and chemical analysis, as well as permeation studies, indicate that high-polarity solvent molecules interact with oxygen functional groups through hydrogen-bonding networks. However, the movement of low-polarity solvents is primarily driven by van der Waals forces in the graphitic regions. Our work highlights the importance of controlling oxygen content in GOMs to optimise transport properties. Our findings are primarily focused on understanding the fundamental interaction between solvents and GO-based membranes through vapor transport behaviour. We believe these insights provide a foundation for the future design of 2D laminated membranes for specific separation applications. This work also highlights the promising characteristics of 2D laminated

membranes, making them attractive candidates for filtration technologies. Beyond this fundamental investigation, further studies on temperature- and pressure-dependent permeation, fully reduced GO membranes with near-zero oxygen content, as well as mixed-solvent systems, can be conducted to enhance the understanding of complex vapor permeation systems and promote the development of high-performance OSN membranes.

CRediT authorship contribution statement

Hongzhe Chen: Writing – review & editing, Writing – original draft, Methodology, Investigation, Data curation, Conceptualization. Tongxi Lin: Writing – review & editing, Writing – original draft, Methodology, Investigation, Conceptualization. Zeno Rizqi Ramadhan: Methodology. Aditya Rawal: Methodology. Yuta Nishina: Methodology, Investigation. Amir Karton: Data curation, Formal analysis, Software, Validation, Visualization, Writing – review & editing. Xiaojun Ren: Writing – review & editing, Writing – original draft, Visualization, Validation, Methodology, Investigation. Rakesh Joshi: Writing – review & editing, Writing – original draft, Visualization, Validation, Supervision, Resources, Project administration, Methodology, Investigation, Formal analysis, Data curation, Conceptualization.

Ethics declarations

The authors declare that they have no known competing financial interests or personal relationships that could have appeared to influence the work reported in this paper.

Declaration of competing interest

The authors declare that they have no known competing financial interests or personal relationships that could have appeared to influence the work reported in this paper.

Acknowledgment

T.L. and X.R. acknowledge the UNSW UIPA Scholarship. The authors acknowledge the staff of the Electron Microscope Unit (EMU) within the Mark Wainwright Analytical Centre (MWAC) at UNSW for technical assistance.

Supporting Information

Supporting Information is available from the Wiley Online Library.

Appendix A. Supplementary data

Supplementary data to this article can be found online at https://doi.org/10.1016/j.carbon.2025.120539.

References

- A. Keerthi, S. Goutham, Y. You, P. Iamprasertkun, R.A.W. Dryfe, A.K. Geim, B. Radha, Water friction in nanofluidic channels made from two-dimensional crystals, Nat. Commun. 12 (2021) 3092, https://doi.org/10.1038/s41467-021-22325
- [2] M. Hu, B. Mi, Enabling graphene oxide nanosheets as water separation membranes, Environ. Sci. Technol. 47 (2013) 3715–3723. https://doi.org/10.1021/es400571g.
- [3] J.Y. Chong, B. Wang, K. Li, Water transport through graphene oxide membranes: the roles of driving forces, Chem. Commun. 54 (2018) 2554–2557, https://doi.org/ 10.1039/C7CC09120F.
- [4] X. Ren, D. Ji, X. Wen, H. Bustamante, R. Daiyan, T. Foller, Y.Y. Khine, R. Joshi, Graphene oxide membranes for effective removal of humic acid, J. Mater. Res. 37 (2022) 3362–3371, https://doi.org/10.1557/s43578-022-00647-6.
- [5] H. Yang, G. Chen, L. Cheng, Y. Liu, Y. Cheng, H. Yao, Y. Liu, G. Liu, W. Jin, Manipulating gas transport channels in graphene oxide membrane with swift heavy ion irradiation, Separ. Purif. Technol. 320 (2023) 124136, https://doi.org/ 10.1016/j.seppur.2023.124136.

- [6] M. Chen, M. Trubyanov, P. Zhang, Q. Wang, Z. Li, K.S. Novoselov, D.V. Andreeva, Comprehensive characterization of gas diffusion through graphene oxide membranes, J. Membr. Sci. (2023) 121583, https://doi.org/10.1016/j. memsci. 2023.121583
- [7] G. Liu, W. Jin, N. Xu, Graphene-based membranes, Chem. Soc. Rev. 44 (2015) 5016–5030, https://doi.org/10.1039/C4CS00423J.
- [8] X. Jin, T. Foller, X. Wen, M.B. Ghasemian, F. Wang, M. Zhang, H. Bustamante, V. Sahajwalla, P. Kumar, H. Kim, G.H. Lee, K. Kalantar-Zadeh, R. Joshi, Effective separation of CO2 using metal-incorporated rGO membranes, Adv. Mater. 32 (2020), https://doi.org/10.1002/adma.201907580.
- [9] M. Joshi, X. Ren, T. Lin, R. Joshi, Mechanistic insights into gas adsorption on 2D materials, Small 21 (2025) 2406706, https://doi.org/10.1002/smll.202406706.
- [10] T. Liu, Y. Li, Q. Du, J. Sun, Y. Jiao, G. Yang, Z. Wang, Y. Xia, W. Zhang, K. Wang, H. Zhu, D. Wu, Adsorption of methylene blue from aqueous solution by graphene, Colloids Surf. B Biointerfaces 90 (2012) 197–203, https://doi.org/10.1016/j.colsurfb.2011.10.019.
- [11] L. Nie, K. Goh, Y. Wang, J. Lee, Y. Huang, H.E. Karahan, K. Zhou, M.D. Guiver, T.-H. Bae, Realizing small-flake graphene oxide membranes for ultrafast size-dependent organic solvent nanofiltration, Sci. Adv. 6 (2020) eaaz9184, https://doi.org/10.1126/sciadv.aaz9184.
- [12] L. Huang, Y. Li, Q. Zhou, W. Yuan, G. Shi, Graphene oxide membranes with tunable semipermeability in organic solvents, Adv. Mater. 27 (2015) 3797–3802, https://doi.org/10.1002/adma.201500975.
- [13] T. Gao, L. Huang, C. Li, G. Xu, G. Shi, Graphene membranes with tuneable nanochannels by intercalating self-assembled porphyrin molecules for organic solvent nanofiltration, Carbon 124 (2017) 263–270, https://doi.org/10.1016/j. carbon.2017.08.042.
- [14] T. Foller, R. Daiyan, X. Jin, J. Leverett, H. Kim, R. Webster, J.E. Yap, X. Wen, A. Rawal, K.K.H.D. Silva, M. Yoshimura, H. Bustamante, S.L.Y. Chang, P. Kumar, Y. You, G.H. Lee, R. Amal, R. Joshi, Enhanced graphitic domains of unreduced graphene oxide and the interplay of hydration behaviour and catalytic activity, Mater. Today 50 (2021) 44–54, https://doi.org/10.1016/j.mattod.2021.08.003.
- [15] K. Erickson, R. Erni, Z. Lee, N. Alem, W. Gannett, A. Zettl, Determination of the local chemical structure of graphene oxide and reduced graphene oxide, Adv. Mater. 22 (2010) 4467–4472, https://doi.org/10.1002/adma.201000732.
- [16] X. Wen, T. Foller, X. Jin, T. Musso, P. Kumar, R. Joshi, Understanding water transport through graphene-based nanochannels via experimental control of slip length, Nat. Commun. 13 (2022) 5690, https://doi.org/10.1038/s41467-022-33456.w
- [17] T. Lin, X. Wen, X. Ren, V. Quintano, D.V. Andreeva, K.S. Novoselov, R. Joshi, Recent advances in graphene-based membranes with nanochannels and nanopores, Small Struct. 6 (2025) 2400320, https://doi.org/10.1002/sstr.202400320.
- [18] J. Shen, G. Liu, Y. Han, W. Jin, Artificial channels for confined mass transport at the sub-nanometre scale, Nat. Rev. Mater. 6 (2021) 294–312, https://doi.org/ 10.1038/s41578-020-00268-7.
- [19] B. Radha, A. Esfandiar, F.C. Wang, A.P. Rooney, K. Gopinadhan, A. Keerthi, A. Mishchenko, A. Janardanan, P. Blake, L. Fumagalli, M. Lozada-Hidalgo, S. Garaj, S.J. Haigh, I.V. Grigorieva, H.A. Wu, A.K. Geim, Molecular transport through capillaries made with atomic-scale precision, Nature 538 (2016) 222–225, https:// doi.org/10.1038/nature19363
- [20] G. Algara-Siller, O. Lehtinen, F.C. Wang, R.R. Nair, U. Kaiser, H.A. Wu, A.K. Geim, I.V. Grigorieva, Square ice in graphene nanocapillaries, Nature 519 (2015) 443–445, https://doi.org/10.1038/nature14295.
- [21] T. Foller, L. Madauß, D. Ji, X. Ren, K.K.H.D. Silva, T. Musso, M. Yoshimura, H. Lebius, A. Benyagoub, P.V. Kumar, M. Schleberger, R. Joshi, Mass transport via In-Plane nanopores in graphene oxide membranes, Nano Lett. 22 (2022) 4941–4948, https://doi.org/10.1021/acs.nanolett.2c01615.
- [22] N. Wei, X. Peng, Z. Xu, Understanding water permeation in graphene oxide membranes, ACS Appl. Mater. Interfaces 6 (2014) 5877–5883, https://doi.org/ 10.1011/cps/00777b
- [23] A. Akbari, S.E. Meragawi, S.T. Martin, B. Corry, E. Shamsaei, C.D. Easton, D. Bhattacharyya, M. Majumder, Solvent transport behavior of shear aligned graphene oxide membranes and implications in organic solvent nanofiltration, ACS Appl. Mater. Interfaces 10 (2018) 2067–2074, https://doi.org/10.1021/ acsami.7b11777.
- [24] Z. Cao, X. Wen, V. Quintano, R. Joshi, On the role of functionalization in graphenemoisture interaction, Curr. Opin. Solid State Mater. Sci. 27 (2023) 101122, https:// doi.org/10.1016/j.cossms.2023.101122.
- [25] T. Foller, R. Joshi, Let's discuss: when can we call a thin film 2-dimensional? Curr. Opin. Solid State Mater. Sci. 32 (2024) 101186 https://doi.org/10.1016/j. cossms.2024.101186.
- [26] K.K.H. De Silva, H.-H. Huang, M. Yoshimura, Progress of reduction of graphene oxide by ascorbic acid, Appl. Surf. Sci. 447 (2018) 338–346, https://doi.org/ 10.1016/j.apsusc.2018.03.243.
- [27] H. Jung, S. Jeon, D.H. Jo, J. Huh, S.H. Kim, Effect of crosslinking on the CO2 adsorption of polyethyleneimine-impregnated sorbents, Chem. Eng. J. 307 (2017) 836–844, https://doi.org/10.1016/j.cej.2016.09.005.
- [28] J. Xu, P. Sang, W. Xing, Z. Shi, L. Zhao, W. Guo, Z. Yan, Insights into the H2/CH4 separation through two-dimensional graphene channels: influence of edge functionalization, Nanoscale Res. Lett. 10 (2015) 492, https://doi.org/10.1186/s11671-015-1199-2.
- [29] L. Huang, J. Chen, T. Gao, M. Zhang, Y. Li, L. Dai, L. Qu, G. Shi, Reduced graphene oxide membranes for ultrafast organic solvent nanofiltration, Adv. Mater. 28 (2016) 8669–8674, https://doi.org/10.1002/adma.201601606.
- [30] S. Zheng, Q. Tu, J.J. Urban, S. Li, B. Mi, Swelling of graphene oxide membranes in aqueous solution: characterization of interlayer spacing and insight into water

- transport mechanisms, ACS Nano 11 (2017) 6440–6450, https://doi.org/10.1021/acsnano.7b02999.
- [31] L. Chen, G. Shi, J. Shen, B. Peng, B. Zhang, Y. Wang, F. Bian, J. Wang, D. Li, Z. Qian, G. Xu, G. Liu, J. Zeng, L. Zhang, Y. Yang, G. Zhou, M. Wu, W. Jin, J. Li, H. Fang, Ion sieving in graphene oxide membranes via cationic control of interlayer spacing, Nature 550 (2017) 380–383, https://doi.org/10.1038/nature24044.
- [32] P. Sun, K. Wang, H. Zhu, Recent developments in graphene-based membranes: structure, mass-transport mechanism and potential applications, Adv. Mater. 28 (2016) 2287–2310, https://doi.org/10.1002/adma.201502595.
- [33] S. Zheng, Q. Tu, M. Wang, J.J. Urban, B. Mi, Correlating interlayer spacing and separation capability of graphene oxide membranes in organic solvents, ACS Nano 14 (2020) 6013–6023, https://doi.org/10.1021/acsnano.0c01550.
- [34] Q. Yang, Y. Su, C. Chi, C.T. Cherian, K. Huang, V.G. Kravets, F.C. Wang, J.C. Zhang, A. Pratt, A.N. Grigorenko, F. Guinea, A.K. Geim, R.R. Nair, Ultrathin graphenebased membrane with precise molecular sieving and ultrafast solvent permeation, Nat. Mater. 16 (2017) 1198–1202, https://doi.org/10.1038/nmat5025.
- [35] S. Guo, S. Garaj, A. Bianco, C. Ménard-Moyon, Controlling covalent chemistry on graphene oxide, Nat Rev Phys 4 (2022) 247–262, https://doi.org/10.1038/ s42254-022-00422-w.
- [36] R.R. Nair, H.A. Wu, P.N. Jayaram, I.V. Grigorieva, A.K. Geim, Unimpeded permeation of water through helium-Leak-Tight graphene-based membranes, Science 335 (2012) 442-444, https://doi.org/10.1126/science.1211694.
- [37] T. Lin, X. Ren, X. Wen, A. Karton, V. Quintano, R. Joshi, Membrane based In-situ reduction of graphene oxide for electrochemical supercapacitor application, Carbon 224 (2024) 119053, https://doi.org/10.1016/j.carbon.2024.119053.
- [38] Y.Y. Khine, X. Wen, X. Jin, T. Foller, R. Joshi, Functional groups in graphene oxide, Phys. Chem. Chem. Phys. 24 (2022) 26337–26355, https://doi.org/10.1039/ D2CP04082D
- [39] Y.Y. Khine, X. Ren, D. Chu, Y. Nishina, T. Foller, R. Joshi, Surface functionalities of graphene oxide with varying flake size, Ind. Eng. Chem. Res. 61 (2022) 6531–6536, https://doi.org/10.1021/acs.iecr.2c00748.
- [40] S. Park, Y. Hu, J.O. Hwang, E.-S. Lee, L.B. Casabianca, W. Cai, J.R. Potts, H.-W. Ha, S. Chen, J. Oh, S.O. Kim, Y.-H. Kim, Y. Ishii, R.S. Ruoff, Chemical structures of hydrazine-treated graphene oxide and generation of aromatic nitrogen doping, Nat. Commun. 3 (2012) 638, https://doi.org/10.1038/ncomms1643.
- [41] N.R. Wilson, P.A. Pandey, R. Beanland, R.J. Young, I.A. Kinloch, L. Gong, Z. Liu, K. Suenaga, J.P. Rourke, S.J. York, J. Sloan, Graphene oxide: structural analysis and application as a highly transparent support for electron microscopy, ACS Nano 3 (2009) 2547–2556, https://doi.org/10.1021/nn900694t.
- [42] J.C. Meyer, A.K. Geim, M.I. Katsnelson, K.S. Novoselov, D. Obergfell, S. Roth, C. Girit, A. Zettl, On the roughness of single- and bi-layer graphene membranes, Solid State Commun. 143 (2007) 101–109, https://doi.org/10.1016/j. ssc.2007.02.047.
- [43] D. Pacilé, J.C. Meyer, A. Fraile Rodríguez, M. Papagno, C. Gómez-Navarro, R. S. Sundaram, M. Burghard, K. Kern, C. Carbone, U. Kaiser, Electronic properties and atomic structure of graphene oxide membranes, Carbon 49 (2011) 966–972, https://doi.org/10.1016/j.carbon.2010.09.063.
- [44] L. Stobinski, B. Lesiak, A. Malolepszy, M. Mazurkiewicz, B. Mierzwa, J. Zemek, P. Jiricek, I. Bieloshapka, Graphene oxide and reduced graphene oxide studied by the XRD, TEM and electron spectroscopy methods, J. Electron. Spectrosc. Relat. Phenom. 195 (2014) 145–154. https://doi.org/10.1016/j.elspec.2014.07.003.
- [45] D.R. Dreyer, S. Park, C.W. Bielawski, R.S. Ruoff, The chemistry of graphene oxide, Chem. Soc. Rev. 39 (2010) 228–240, https://doi.org/10.1039/B917103G.
- [46] Y. Cao, Z. Xiong, Q. Liang, W.-J. Jiang, F. Xia, X. Du, L. Zu, S. Mudie, G.V. Franks, D. Li, Subnanometric stacking of two-dimensional nanomaterials: insights from the nanotexture evolution of dense reduced graphene oxide membranes, ACS Nano 17 (2023) 5072–5082, https://doi.org/10.1021/acsnano.3c00155.
- [47] G. Eda, G. Fanchini, M. Chhowalla, Large-area ultrathin films of reduced graphene oxide as a transparent and flexible electronic material, Nat. Nanotechnol. 3 (2008) 270–274, https://doi.org/10.1038/nnano.2008.83.
- [48] A.C. Ferrari, J.C. Meyer, V. Scardaci, C. Casiraghi, M. Lazzeri, F. Mauri, S. Piscanec, D. Jiang, K.S. Novoselov, S. Roth, A.K. Geim, Raman spectrum of graphene and graphene layers, Phys. Rev. Lett. 97 (2006) 187401, https://doi.org/10.1103/PhysRevLett.97.187401.
- [49] A. Kaniyoor, S. Ramaprabhu, A Raman spectroscopic investigation of graphite oxide derived graphene, AIP Adv. 2 (2012) 032183, https://doi.org/10.1063/ 1.4756995.
- [50] A. Sadezky, H. Muckenhuber, H. Grothe, R. Niessner, U. Pöschl, Raman microspectroscopy of soot and related carbonaceous materials: spectral analysis and structural information, Carbon 43 (2005) 1731–1742, https://doi.org/ 10.1016/j.carbon.2005.02.018.
- [51] Y. Cao, Z. Xiong, F. Xia, G.V. Franks, L. Zu, X. Wang, Y. Hora, S. Mudie, Z. He, L. Qu, Y. Xing, D. Li, New structural insights into densely assembled reduced graphene oxide membranes, Adv. Funct. Mater. 32 (2022) 2201535, https://doi. org/10.1002/adfm.202201535.
- [52] X. Díez-Betriu, S. Álvarez-García, C. Botas, P. Álvarez, J. Sánchez-Marcos, C. Prieto, R. Menéndez, A. De Andrés, Raman spectroscopy for the study of reduction mechanisms and optimization of conductivity in graphene oxide thin films, J. Mater. Chem. C 1 (2013) 6905, https://doi.org/10.1039/c3tc31124d.
- [53] D. López-Díaz, M. López Holgado, J.L. García-Fierro, M.M. Velázquez, Evolution of the raman spectrum with the chemical composition of graphene oxide, J. Phys. Chem. C 121 (2017) 20489–20497, https://doi.org/10.1021/acs.jpcc.7b06236.
- [54] S. Kanehashi, K. Nagai, Gas and vapor transport in membranes, in: Membrane Characterization, Elsevier, 2017, pp. 309–336, https://doi.org/10.1016/B978-0-444-63776-5.00014-0.
- [55] R. Baker, Membrane Technology and Applications, 2004.

- [56] R.K. Joshi, P. Carbone, F.C. Wang, V.G. Kravets, Y. Su, I.V. Grigorieva, H.A. Wu, A. K. Geim, R.R. Nair, Precise and ultrafast molecular sieving through graphene oxide membranes, Science 343 (2014) 752–754, https://doi.org/10.1126/science.1245711.
- [57] Y. Zhao, D.G. Truhlar, Design of density functionals that are broadly accurate for thermochemistry, thermochemical kinetics, and nonbonded interactions, J. Phys. Chem. A 109 (2005) 5656–5667, https://doi.org/10.1021/jp050536c.
- [58] S. Grimme, S. Ehrlich, L. Goerigk, Effect of the damping function in dispersion corrected density functional theory, J. Comput. Chem. 32 (2011) 1456–1465, https://doi.org/10.1002/jcc.21759.
- [59] F. Weigend, R. Ahlrichs, Balanced basis sets of split valence, triple zeta valence and quadruple zeta valence quality for H to Rn: design and assessment of accuracy, Phys. Chem. Chem. Phys. 7 (2005) 3297, https://doi.org/10.1039/b508541a.
- [60] N. Mehta, T. Fellowes, J.M. White, L. Goerigk, CHAL336 benchmark set: how well Do quantum-chemical methods describe chalcogen-bonding interactions? J. Chem. Theor. Comput. 17 (2021) 2783–2806, https://doi.org/10.1021/acs.jctc.1c00006.
- [61] A.A. Kroeger, A. Karton, π-π catalysis in carbon Flatland—flipping [8]Annulene on graphene, Chem. Eur J. 27 (2021) 3420–3426, https://doi.org/10.1002/ chem.202004045.
- [62] A.A. Kroeger, A. Karton, Catalysis by pure graphene—From supporting actor to protagonist through shape complementarity, J. Org. Chem. 84 (2019) 11343–11347, https://doi.org/10.1021/acs.joc.9b01909.

- [63] L. Goerigk, A. Hansen, C. Bauer, S. Ehrlich, A. Najibi, S. Grimme, A look at the density functional theory zoo with the advanced GMTKN55 database for general main group thermochemistry, kinetics and noncovalent interactions, Phys. Chem. Chem. Phys. 19 (2017) 32184–32215, https://doi.org/10.1039/C7CP04913G.
- [64] R. Sure, S. Grimme, Comprehensive benchmark of association (free) energies of realistic host-guest complexes, J. Chem. Theor. Comput. 11 (2015) 3785–3801, https://doi.org/10.1021/acs.jctc.5b00296.
- [65] S. Grimme, Supramolecular binding thermodynamics by dispersion-corrected density functional theory, Chem. Eur J. 18 (2012) 9955–9964, https://doi.org/ 10.1002/chem.201200497.
- [66] L. Goerigk, S. Grimme, A thorough benchmark of density functional methods for general main group thermochemistry, kinetics, and noncovalent interactions, Phys. Chem. Chem. Phys. 13 (2011) 6670, https://doi.org/10.1039/c0cp02984j.
- [67] A. Karton, D. Gruzman, J.M.L. Martin, Benchmark thermochemistry of the C_n H_{2 n} +2 alkane isomers (n=2-8) and performance of DFT and composite Ab initio methods for dispersion-driven isomeric equilibria, J. Phys. Chem. A 113 (2009) 8434–8447, https://doi.org/10.1021/jp904369h.
- [68] A. Karton, A. Tarnopolsky, J.-F. Lamère, G.C. Schatz, J.M.L. Martin, Highly accurate first-principles benchmark data sets for the parametrization and validation of density functional and other approximate methods. Derivation of a robust, generally applicable, double-hybrid functional for thermochemistry and thermochemical kinetics, J. Phys. Chem. A 112 (2008) 12868–12886, https://doi.org/10.1021/jp801805p.